Imaging Light-Induced Migration of Dislocations in Halide Perovskites with 3d Nanoscale Strain Mapping

*Kieran W. P. Orr, Jiecheng Diao, Muhammad Naufal Lintangpradipto, Darren J. Batey, Affan N. Iqbal, Simon Kahmann, Kyle Frohna, Milos Dubajic, Szymon J. Zelewski, Alice E. Dearle, Thomas A. Selby, Peng Li, Tiarnan A. S. Doherty, Stephan Hofmann, Osman M. Bakr, Ian K. Robinson, and Samuel D. Stranks**

In recent years, halide perovskite materials have been used to make high-performance solar cells and light-emitting devices. However, material defects still limit device performance and stability. Here, synchrotron-based Bragg coherent diffraction imaging is used to visualize nanoscale strain fields, such as those local to defects, in halide perovskite microcrystals. Significant strain heterogeneity within $MAPbBr_3$ ($MA = CH_3NH_3^+$) crystals is found in spite of their high optoelectronic quality, and both ⟨100⟩ and ⟨110⟩ edge dislocations are identified through analysis of their local strain fields. By imaging these defects and strain fields in situ under continuous illumination, dramatic light-induced dislocation migration across hundreds of nanometers is uncovered. Further, by selectively studying crystals that are damaged by the X-ray beam, large dislocation densities and increased nanoscale strains are correlated with material degradation and substantially altered optoelectronic properties assessed using photoluminescence microscopy measurements. These results demonstrate the dynamic nature of extended defects and strain in halide perovskites, which will have important consequences for device performance and operational stability.

1. Introduction

Halide perovskites are promising materials for highly efficient optoelectronic devices. In under a decade, the power conversion efficiency of halide perovskite-based single junction solar cells has increased from 14.1% (2013)[1] to 26.1% (2023),[2] and efficiencies of 33.7% have been reported for perovskite/Si tandem devices.[2] Additionally, external quantum efficiencies have risen sharply to 28.9% for perovskite-based green light emitting diodes (LEDs),[3] with blue, red, and near-infrared analogues also with reported efficiencies over 20%.[4–6] In spite of being a younger field, there have also been tremendous successes using halide perovskites as X-ray detectors.[7,8] This prodigious rise in device efficiency and applications has, in large part, been achieved through empirical optimization of device processing, and the

K. W. P. Orr, A. N. Iqbal, S. Kahmann, K. Frohna, M. Dubajic, S. J. Zelewski, A. E. Dearle, T. A. Selby, T. A. S. Doherty, S. D. Stranks
Department of Chemical Engineering and Biotechnology
University of Cambridge
Philippa Fawcett Drive, Cambridge CB3 0AS, UK
E-mail: sds65@cam.ac.uk

K. W. P. Orr, A. N. Iqbal, S. Kahmann, K. Frohna, S. J. Zelewski, A. E. Dearle, T. A. S. Doherty, S. D. Stranks
Department of Physics
Cavendish Laboratory
University of Cambridge
JJ Thomson Avenue, Cambridge CB3 0HE, UK

The ORCID identification number(s) for the author(s) of this article can be found under https://doi.org/10.1002/adma.202305549

[+]Present address: Center for Transformative Science, ShanghaiTech University, Shanghai 201210, China

DOI: 10.1002/adma.202305549

J. Diao[+], I. K. Robinson
London Centre for Nanotechnology
University College London
London WC1E 6BT, UK

M. N. Lintangpradipto, O. M. Bakr
KAUST Catalysis Center (KCC)
Division of Physical Sciences and Engineering (PSE)
King Abdullah University of Science and Technology (KAUST)
23955-6900 Thuwal, Kingdom of Saudi Arabia

D. J. Batey, P. Li
Diamond Light Source
Harwell Science and Innovation Campus
Fermi Ave, Didcot OX11 0DE, UK

A. E. Dearle, S. Hofmann
Department of Engineering
University of Cambridge
Cambridge CB2 1PZ, UK

T. A. S. Doherty
Department of Materials Science & Metallurgy
University of Cambridge
27 Charles Babbage Road, Cambridge CB3 0FS, UK

I. K. Robinson
Condensed Matter Physics and Materials Science Department
Brookhaven National Lab
Upton, New York 11793, USA

community's fundamental understanding of halide perovskite materials, especially the impact of nanoscale structure, lags behind device performance enhancements.

One aspect of material structure that is poorly understood in halide perovskites (compared to traditional semiconductors) is strain, which has been proposed to affect carrier lifetime,[9] bandgap,[10] Urbach energy,[11] ion migration,[12] material stability,[12,13] as well as overall device efficiency.[14] In the halide perovskite field, strain is most commonly characterized by assessing Bragg peak shifts (tensile and compressive strain[9–11]) or Bragg peak broadening (microstrain[15]) which evaluate the linear expansion of the material and *d*-spacing disorder, respectively. Perovskite thin films used in optoelectronic devices are generally under biaxial tensile strain due to the thermal expansion mismatch between perovskite and glass substrates inhibiting perovskite contraction in the in-plane directions after annealing.[16,17] However, the distribution of strain in most films is also spatially heterogeneous across a range of length scales, from a few nanometers up to hundreds of micrometers.[18] Further, there are additional vertical strain gradients across the film thickness[10] as the effect of the substrate reduces further away from the interface. Therefore, to obtain a full understanding of strain in halide perovskites and its impact on performance, one must characterize strain on a local scale and in three dimensions. In general, the techniques outlined above probe the average structure of the material bulk, and, even when employing synchrotron nano-probe facilities, it is difficult to achieve a spatial resolution (spot size) below ≈10 nm.[19] Furthermore, the structure of the perovskite in devices evolves during operation, as evidenced by decreasing efficiencies over time. As such, it is important to study material structure under operational stressors in situ to understand modes of device degradation and failure.

A full description of strain in materials (structural deformation due to applied stress) is derived from atomic displacement vectors, $\boldsymbol{u}(\boldsymbol{r})$ (where $\boldsymbol{r}$ is a real space position vector), which describe the amount by which atoms are displaced from their expected positions according to the underlying lattice. Interrogation of atomic displacements allows one to identify point defects and dislocations from their characteristic local strain fields, providing unparalleled insight into the internal structure of materials. ⟨100⟩ edge dislocations have been reported in the halide perovskite $FAPbI_3$[20] ($FA = CH(NH_2)_2^+$) and $\frac{1}{2}\langle 110\rangle$ screw dislocations have been identified in $CsPbBr_3$,[21] both using atomic-resolution scanning transmission electron microscopy (STEM). However, STEM and related electron microscopy techniques generally require the use of thin samples (<< 10 nm), rendering them of limited use for imaging buried dislocations in crystals relevant to optoelectronic devices. Electron tomography, while able to image dislocations in semiconductors in 3D,[22] uses beam doses that are prohibitively high for halide perovskites.

Bragg coherent diffraction imaging (BCDI) measurements can provide information on atomic displacement vectors with nanometer resolution in thicker samples, such as those that may be used in optoelectronic devices. The technique has been employed to reveal the 3D atomic displacement fields within ZnO nanorods,[23] to track the evolution of ferroelastic domain walls in barium titanate,[24] and to identify twin domains in $CsPbBr_3$ nanoparticles.[25] Further, the approach has been used to monitor the growth of crystalline grains during the annealing process of In_2O_3:Zr thin films,[26] during calcite crystal solution and dissolution,[27] and to track dislocations dynamics in the $LiNi_{0.5}Mn_{1.5}O_4$ battery electrode material during charging and discharging.[28]

Here, we develop an in situ BCDI approach to visualize the surprisingly rich strain fields within high-quality single microcrystals of halide perovskites and monitor their evolution under continuous solar illumination. By tracking the strain fields in $MAPbBr_3$, we identify ⟨100⟩ and ⟨110⟩ edge dislocations and observe their surprisingly extensive migration through the crystal structure under illumination. By considering crystals that become damaged under X-ray exposure, we also find dislocation formation to be associated with degradation of the halide perovskite material and changes in its optoelectronic properties. These findings give mechanistic insight into the structural evolution of halide perovskites under operating conditions, and identify the important role extended defects and nanoscale strain play in device performance and operational stability of solar cells, photodetectors, LEDs, and X-ray detectors made from these materials.

2. Results and Discussion

2.1. Imaging Nanoscale Strain with Bragg Coherent Diffraction Imaging

For these studies, we employ high-quality $MAPbBr_3$ microcrystals of 1–3 μm in size recently used in high-performing photodetectors,[29,30] with scanning electron micrographs (SEM) of representative microcrystals shown in Figures 1c,d (microcrystal films and isolated microcrystals, respectively). In this study, we focus on the canonical $MAPbBr_3$ composition, so that any strains observed are not due to compositional heterogeneity, as might be the case in alloyed perovskites with mixed cations on the A-site or mixed halides on the X-site. BCDI is a lensless imaging technique that involves illuminating a sample with a coherent beam of X-rays from a synchrotron source. When the diffracting object is the same size or smaller than the lateral coherence length of the X-ray beam, a coherent X-ray diffraction pattern can be recorded that includes extra interference fringes seen around each of the Bragg peaks. An example coherent diffraction pattern is shown on the detector in **Figure 1**a. From a set of these patterns, collected at different sample rocking angles, a three-dimensional electron density function $\rho(\boldsymbol{r})$ can be reconstructed using an iterative phase retrieval algorithm, details of which are given in the Methods and elsewhere.[31–33] Additional information about BCDI is given in Supporting Note 1 in the Supporting Information. In general, $\rho(\boldsymbol{r})$ is complex-valued, with the modulus proportional to the crystal's electron density and the argument proportional to the size of the atomic displacement along the direction of the X-ray scattering vector, $\boldsymbol{Q}$.[34,35] To a first-order approximation, the size and shape of the diffracting crystal can be extracted from the interference fringe spacing around the outside of the Bragg peak, and the strain information is contained in the intensity asymmetry near the center of the peak.[34] Figure 1b shows a 3D rendering of the reconstructed electron density of an example $MAPbBr_3$ microcrystal. Henceforth, such electron density renderings will be referred to simply as "reconstructions".

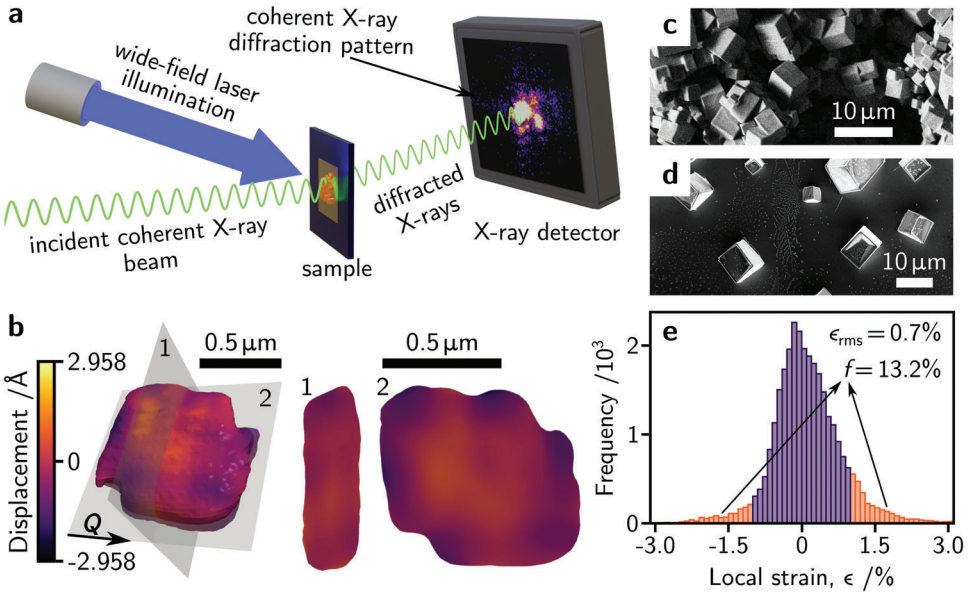

Figure 1. BCDI enables reconstruction of strain fields in halide perovskite microcrystals: a) Schematic of the BCDI measurement geometry. A coherent beam of X-rays is incident from the left and is diffracted by crystals on the sample towards a detector that records a coherent X-ray diffraction pattern. A laser mounted on the beamline provides wide-field visible light illumination with a wavelength of 405 nm. b) Example electron density reconstruction of a $MAPbBr_3$ microcrystal (left), with slices through the 3D volume indicated by the numbered grey planes (middle and right). The colour scale of c) a microcrystal film (continuous films made up of many touching microcrystals) and d) isolated $MAPbBr_3$ microcrystals. e) Histogram of local nanoscale tensile (positive) and compressive (negative) strain for the crystal shown in panel b). Local strain values exceeding a magnitude of 1% are highlighted in orange. The root mean squared local strain, ε_{rms}, and fraction of the crystal volume with local strain exceeding 1%, f, are quoted.

Two perpendicular slices taken through the reconstruction are also shown in Figure 1b and the color scale indicates the size of the atomic displacement along the scattering vector direction.

By taking the spatial derivative of the displacement field of the reconstruction shown in Figure 1b with respect to the direction of the scattering vector, we obtain values for the local nanoscale tensile (positive) and compressive (negative) strain between voxels of the reconstruction. These values correspond to one of the local diagonal elements of the microscopic strain tensor. Figure 1e shows a histogram of these local strain values for the crystal in Figure 1b, with those of magnitude greater than 1% highlighted in orange. For this crystal, the fraction of the crystal volume with local strain exceeding 1%, f, is 13.2%, and the root mean squared value of local strain, ε_{rms}, is 0.7%. These values are relatively low when compared to those for other (undamaged) crystals in this study, for which we find $5\% < f < 30\%$ and $0.5\% < \varepsilon_{rms} < 4.5\%$ (see Table S1, Supporting Information). Such strain values are remarkably high since halide perovskites prepared in this manner are used in high-performing devices.[30] By contrast, devices based on Si[36] and $Cu(In,Ga)Se_2$[37] suffer significant performance losses after strain exceeds ≈1%. Such an observation links closely to the apparent defect tolerance of halide perovskites, where such large strains are not catastrophic for optoelectronic performance.

2.2. Characterizing Dislocations in Halide Perovskites

Dislocations can be identified in reconstructions from a core of low electron density surrounded by a characteristic displacement field.[24] **Figure 2**a shows a reconstruction of a $MAPbBr_3$ microcrystal rendered in grey and made partially transparent to facilitate the identification of a dislocation, which is highlighted with a black line. An infinitesimally thin slice through this reconstruction, perpendicular to the dislocation, is colored according to the atomic displacements and is shown in the reconstruction in Figure 2a, and face-on in Figure 2b.

In Figure 2c, we show the displacement values as a function of arc angle, θ, here defined as zero at minimum atomic displacement (traveling in a circle around the dislocation core shown by the white arrow in Figure 2b). The periodic modulation of the displacement superimposed on a linear trend indicates that the dislocation present is an edge dislocation (as opposed to a screw dislocation),[38] which is shown schematically in Figure 2d. The Burgers vector, $\boldsymbol{b}$, describes the lattice distortion caused by a dislocation[38] and is represented by the green arrow in Figure 2d. To determine the magnitude of the Burgers vector, $|\boldsymbol{b}|$, we fit the displacement versus arc angle data shown in Figure 2c according to the function[24,28,39]

$$u = \frac{|b|}{2\pi}\left(\theta + \frac{\sin(2\theta) - \cos(2\theta)}{4(1-\nu)} + \frac{(2\nu-1)}{2(1-\nu)}\log(r)\right) \quad (1)$$

where u is the size of the atomic displacement (i.e., $u = \boldsymbol{u}(\boldsymbol{r}) \cdot \boldsymbol{Q}$), ν is the Poisson's ratio of the material (taken to be 0.29[40]), and r is the radius of the circle from which we extract the data (see Methods for more details of calculation). For this dislocation, we find $|\boldsymbol{b}| = 5.44$ Å, which is close to the lattice parameter, $d_{100} = 5.92$ Å (an average of literature values[41–43]). Therefore, we conclude that this dislocation is a ⟨100⟩ edge dislocation.

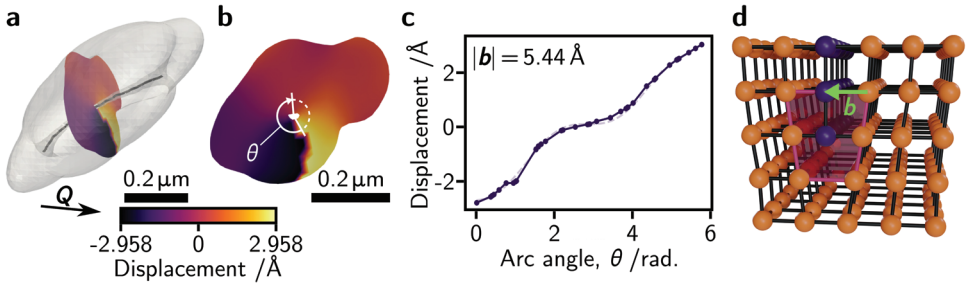

Figure 2. Visualising buried edge dislocations in a $MAPbBr_3$ crystal: a) Electron density reconstruction shown partially transparent in grey, with a ⟨100⟩ edge dislocation indicated by the black line. A slice through the reconstruction is shown coloured according to the size of the atomic displacement along the direction of the scattering vector. b) The slice from a) shown face-on. c) Points and solid line: The atomic displacements as a function of arc angle (indicated by the white arrow in b). Dashed line: fit to data of the function for atomic displacement, u. d) Schematic representation of an edge dislocation. The atoms in purple belong to an extra atomic plane in the top three rows of the structure. The region in pink highlights the highly strained region in the vicinity of the dislocation and the green arrow is the Burgers vector, $\boldsymbol{b}$.

Other possible edge dislocations would involve the insertion of lattice planes with smaller interplanar spacings, for example, a ⟨110⟩ dislocation with $|\boldsymbol{b}| = d_{110} = 4.19$ Å, or a ⟨111⟩ dislocaiton with $|\boldsymbol{b}| = d_{111} = 3.42$ Å, which are in significantly worse agreement with a Burgers vector magnitude of 5.44 Å.

We note that the reconstruction shown in Figure 2b is not as well-faceted as that shown in Figure 1b (i.e., the reconstruction in Figure 2b does not show large, well-defined, flat surfaces reflecting the symmetry of the underlying crystal structure), and the reconstructions appear less well-faceted than expected from the cuboidal crystal shapes in the SEM images (Figures 1c,d). Regions of the crystal that are off Bragg condition will not diffract any X-rays to the detector, and so any void regions are likely due to parts of the crystal being twisted into a slightly different orientation, or that are amorphous. Such twisting of the underlying lattice has been reported for halide perovskites; for example, intra-grain orientational heterogeneity has been confirmed from electron backscatter diffraction in $MAPbI_3$[44] (see Supporting Note 2 and Figure S1, Supporting Information). Where reconstructions from multiple scans are shown (for example in **Figure 3**), unless stated otherwise, the diffracted intensity remains constant for each scan, indicating that these missing volumes are not caused by beam damage.

2.3. Light-Induced Dislocation Migration

To understand the nanoscale structural behavior under device-like conditions, we now consider the evolution of the strain fields in the halide perovskite crystals under continuous visible illumination. In Figure 3a we show a reconstruction of a crystal with a bright, structured Bragg peak that was radiation-stable, i.e., the Bragg peak has the same intensity, and is at the same position in reciprocal space (same rocking curve angle) for each successive scan. Supporting Note 3 and Figures S2–S4 in the Supporting Information, and Supporting Video S1 discuss beam stability in further detail. Having found such a crystal, we illuminate the sample with a 405 nm laser at an intensity of ≈1 sun intensity (in terms of photo-generated charge carriers) and simultaneously acquire further BCDI measurements at different time snapshots. Figures 3b–e show reconstructions of this crystal under continuous illumination with dislocations highlighted in black; each of these dislocations also have Burgers vector magnitudes $\simeq d_{100} = 5.92$ Å (Figures S8–S12, Supporting Information). Under continued illumination, the dislocation mobility increases strikingly, with dislocations moving hundreds of nanometers through the crystal in minutes compared to our control scans, where successive measurements taken in the dark show the dislocation to be

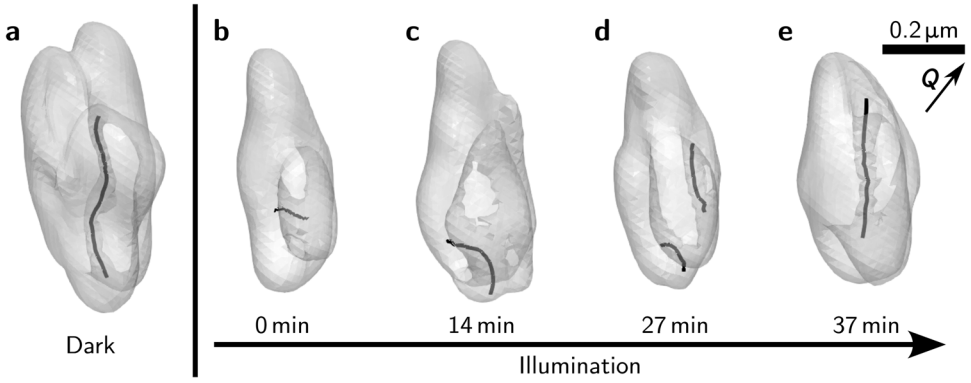

Figure 3. Tracking dislocation migration in a $MAPbBr_3$ microcrystal in situ under illumination: Electron density reconstructions of a $MAPbBr_3$ microcrystal from successive BCDI scans. a) Reconstruction of the crystal in dark conditions. b,c,d,e) Reconstructions of the crystal after continuous illumination with a 405 nm laser at different times. Times given are relative to the start of the BCDI scan giving the reconstruction in b. There were 105 min of illumination between a) and b) for re-optimisation of scan parameters after starting illumination. Dislocations are shown in black and appear very mobile under illumination. The scale bar and scattering vector apply to all reconstructions.

consistently along the long axis of the crystal (Figure S2, Supporting Information). Thus, we are able to image for the first time the increased migration of such nanoscale extended defects in halide perovskites under visible light illumination. Our result is also consistent with reports showing that ions can migrate more easily under illumination in these materials[45–49]; while dislocations can migrate large distances with only small ion motions, ions must still rearrange to effect dislocation migration. These results, tracking the migration of buried dislocations in high-performance halide perovskites, show their internal structure to be remarkably dynamic under operational conditions.

As the dislocations migrate through the crystal under continued illumination, the dislocations curve and take on screw-like character (***b*** parallel to dislocation line) as well as edge-like character (***b*** perpendicular to dislocation line), while maintaining a Burgers vector of $|\boldsymbol{b}| \simeq 5.92$ Å. This observation is also reflected in the more linear appearance of displacement versus arc angle plots for some of these dislocations (Figure S8–S12, Supporting Information), since a pure screw dislocation would give a straight line, whereas a pure edge dislocation would yield a sinusoidally varying graph. The dislocations also move in three dimensions, i.e., not just within a 2D glide plane for a perfect edge dislocation, providing further evidence for the dislocations' mixed character as they evolve and/or evidence of a high density of point defects which may allow the dislocations to climb perpendicular to their glide planes (see Supporting Video S2 for further visualization of the dislocation movement). The dislocations shown in each reconstruction are not necessarily the same as those in the previous reconstruction. Dislocations may migrate to the surface of the crystal where they are annihilated, they may grow in from the crystal surface, a single dislocation may split into new ones, or multiple dislocations may combine with/annihilate each other (so long as the sum of Burgers vectors is conserved). We note that the volume of the reconstructions shown in Figure 3 also decreases upon illumination (Figure S13, Supporting Information). After BCDI measurements, the crystals are still the same shape (well-faceted) when viewed under PL microscopes with no obvious decrease in size (Figure S14, Supporting Information), and therefore we attribute the voids of electron density to regions of the crystals that no longer satisfy the same Bragg condition,[50] possibly due to some photo-induced change in orientation of these regions of the crystal, such as that reported for the related $MAPbI_3$ perovskite.[51] The mechanism of such light-induced reorientation is not well understood and is the subject of current work. It is possible that, since illumination reduces the activation barrier to ion migration,[45–49] the crystal structure is more able to reorient itself as a relaxation mechanism in response to local stress. Light can change the energy landscape of other defects in halide perovskites, for example destabilizing Frenkel defect pairs relative to the perfect crystal structure in $MAPbI_3$.[52] An analogous mechanism could be at play here, favoring certain crystallographic orientations over others once the system is excited with incident light. Illumination may also cause point defect formation (again, as it does in $MAPbI_3$[53]) which will reduce the structure factor of the crystal, resulting in a smaller reconstructed volume. Further studies spurred on from this work will uncover the precise mechanisms involved.

2.4. Optoelectronic Changes upon Dislocation Formation

In order to understand links between dislocations, performance, and degradation in halide perovskites, we now specifically consider crystals that suffer beam damage during measurement. For these crystals, measurements were carried out using a different, more damaging beam energy of 9.7 keV (as opposed to 11.8 keV for results presented above), and successive scans exhibited lower diffracted intensity indicating a smaller crystal volume on the Bragg condition and/or increasing disorder or point defects in the sample. Reconstructions of such a crystal are shown in **Figure 4**a–d (see Supporting Video S3 for additional views of the reconstructions). Upon the second exposure to X-rays, the crystal becomes less well-faceted and more strained, as can be seen from the larger and more dramatic changes in color (atomic displacement). A particularly striking structural change is the formation of a network of many dislocations upon degradation. The majority of these dislocations have Burgers vector magnitudes $\simeq d_{100} = 5.92$ Å, as before (Figures S15–S22, Supporting Information), but we also identify a dislocation with a Burgers vector of magnitude 4.31 Å $\simeq d_{110}$ which connects two ⟨100⟩ dislocations and is highlighted in the inset of Figure 4d. We show another example of a crystal that suffers beam damage causing dislocation formation in Figures S23 and S24 in the Supporting Information, and in Supporting Information Video S4.

To understand the effects of the increased nanoscale strain and dislocation density in these crystals, we conducted wide-field hyperspectral photoluminescence (PL) microscopy and time-resolved confocal PL microscopy measurements on the same sample regions before and after exposure to X-rays. The crystals studied that suffered beam damage existed in an 18 μm × 18 μm region that was repeatedly exposed to the X-ray beam during the synchrotron experiment and that overlaps with one of these pre-mapped areas (Figure 4e inset). By summing the PL from this region of the sample before and after the X-ray measurements we find that the damaged crystals have a peak PL emission at 531 nm compared to a value of 541 nm for the pristine crystals (Figure 4e, see PL peak emission wavelength maps in Figure S25 of the Supporting Information). Further, we see an increase in PL lifetime for a representative crystal before and after X-ray exposure, with the time taken to fall to 1/e of the initial intensity being 1.05 ns for pristine crystals and 1.9 ns for damaged crystals (Figure 4f). Excitation fluences of 78 nJ cm^{-2} and 194 nJ cm^{-2} were used for PL decay measurements on pristine and damaged crystals, respectively, but the difference in PL lifetime observed is much greater than that caused by fluence differences (Figure S26, Supporting Information). Such optoelectronic changes could be caused by the formation of isolated nano-sized confined crystallites on the surface of the crystals, or degradation-induced passivation, for example through the formation of $PbBr_2$ (beam-induced $PbBr_2$ formation has been reported for the related $(FA_{0.79}MA_{0.16}Cs_{0.05})Pb(I_{0.83}Br_{0.17})_3$ system).[54]

While we cannot unambiguously decouple the contributions to the changes in PL characteristics from strain and increased dislocation density, the structural changes characterized here – dislocation formation, increased strain, a significant increase in both f (13.2% to 48.0%) and ε_{rms} (1.0% to 5.1%), reduction in crystallite volume – clearly correlate with changes in

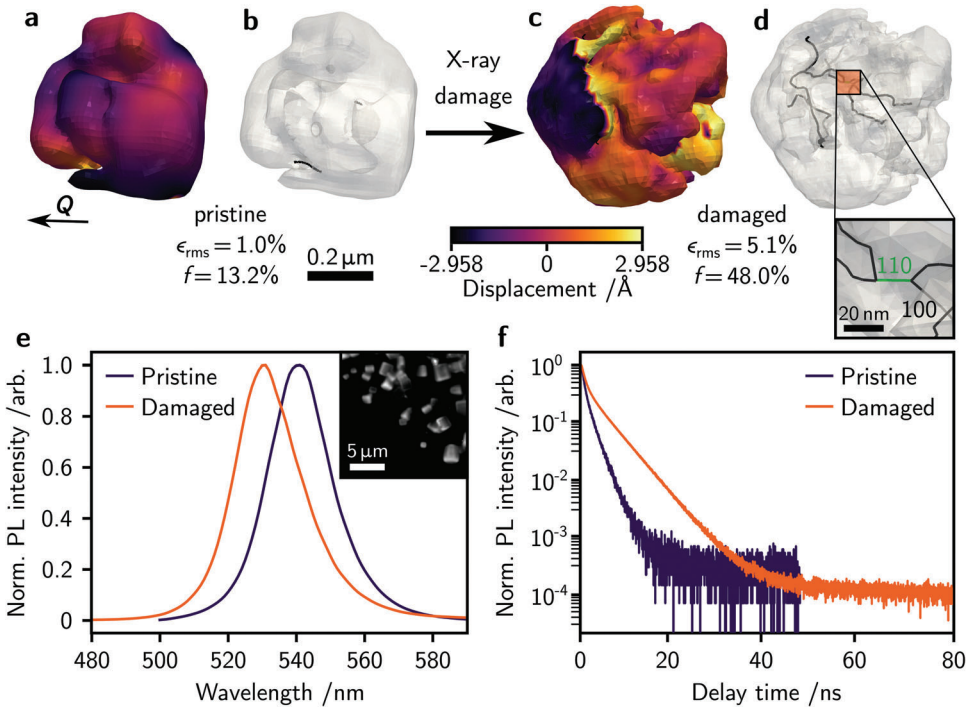

Figure 4. Impact of dislocation density on optoelectronic properties: Electron density reconstructions of a a,b) crystal from its first BCDI scan and c,d) from its second scan. Reconstructions are shown coloured according to the size of the atomic displacement along the direction of the scattering vector (a, c), and partially transparent in solid grey (b, d). Dislocations are shown as black lines. Exposure to X-rays damages the crystals, causing dislocation formation and increased strain (more dramatic changes in atomic displacement vector). The scale bar applies to all reconstructions. e) PL spectra and f) PL decays summed from pristine and damaged crystals upon excitation with a 509 nm laser using an excitation fluence of 78 nJ cm^{-2} for the pristine crystals and 194 nJ cm^{-2} for the damaged crystals.

optoelectronic properties. These results have significant implications for the halide perovskites used in devices for photodetection[29] and direct X-ray detection[55] because dislocations may contribute to nonradiative recombination, afterglow/fall time, responsivity, and parasitic absorption.[29,56]

2.5. Comparisons to Other Semiconductors

Dislocation formation and migration are important mechanisms for strain relaxation in materials. For example, edge dislocations are known to form in epitaxial films of $CaCO_3$ under tensile stress beyond a critical layer thickness.[57] Considering that the vast majority of halide perovskite thin films are under tensile strain because of the high film annealing temperatures and the mismatch in thermal expansion properties between the perovskite and the substrate,[16,58] we expect the light-induced formation and migration of these edge dislocations to be a strain relief mechanism active in working devices.

Further, there is rich dislocation formation and migration behavior in semiconductors such as silicon and gallium pnictogenides, where dislocations also interact with localized (point) defects present in the crystals (though these studies do not consider the effect of visible light illumination).[59,60] The face-centered cubic (FCC) structure is shared by Si, the anion sublattice of gallium pnictogenides, and the halide sublattice in many halide perovskites, with them each in turn sharing similar dislocation behavior. Anderson et al.[39] note the stability of dislocations with a $|\boldsymbol{b}|$ of $\frac{1}{2}\langle 110\rangle$ and $\langle 100\rangle$ for FCC systems in general. $\frac{1}{2}\langle 110\rangle$ dislocations are commonly observed in Si,[61,62] GaN,[63] GaP,[64,65] and GaAs,[66] and both $\frac{1}{2}\langle 110\rangle$ and $\langle 100\rangle$ dislocations have been found in $FAPbI_3$.[20] Here, we demonstrate that $\langle 100\rangle$ dislocations are common in $MAPbBr_3$ and that $\langle 110\rangle$ can also be found. Crucially, we also demonstrate the increased mobility of these dislocations under visible light illumination with nanometer resolution, giving unprecedented access to the buried structural changes occurring during device operation. Increased dislocation migration under infra-red irradiation has been reported in germanium crystals, but this was assessed by tracking the migration of dislocation rosettes on the surface of crystals that had been intentionally indented.[67] Our study uniquely tracks the migration of buried dislocations that result from common solution-processed synthesis methods. Halide ions are the most mobile species in halide perovskites,[45] therefore, one would expect them to be involved in dislocation migration. Given that the dislocations identified in this work are isostructural to those found in other FCC systems, we conclude that it is likely that the ions of the FCC halide sublattice move to realize dislocation migration. The mobility of dislocations in such high-performance semiconductors is surprising considering similar behavior is seen in the highly disordered $LiNi_{0.5}Mn_{1.5}O_4$ battery electrode material during cycling,[28] and calcite crystals during crystal growth and dissolution.[27] Ion movements with low activation barriers are fundamental to the electrochemistry and crystal growth

processes at play in these studies, but are normally detrimental to the performance of traditional semiconductors in devices.

Dislocations in semiconductors are generally sites of nonradiative recombination, causing phonon emission into the lattice which may help dislocations overcome their activation barrier to migration in the recombination-enhanced defect reaction (REDR) mechanism.[68] Detailed temperature- and fluence-dependent measurements are needed to describe REDR in halide perovskites and illumination-coupled nanoindentation measurements may also be required to assess the effects of possible photoplastic effects.[69] The dangling bonds at the end of the additional atomic plane in an edge dislocation can act as donors and/or acceptors of electrons,[70] with the exact donating or accepting character determined by the plane termination (in this case, if the dangling bonds are on Br, Pb or MA). For a neutral dislocation, a half-filled one-dimensional band is expected to form in the bandgap of the bulk material,[68] which can split to lower the system's electronic energy following distortion of the dislocation core in a fashion analogous to a Peierls transition.[71] BCDI cannot yet offer the resolution required to determine the precise atomic structure at the core of a dislocation necessary for understanding its electronic nature (donating/accepting, band structure, capture cross-section, etc.). Atomic resolution electron diffraction techniques and modeling may be able to provide the required atomic configurations and electron paramagnetic resonance spectroscopy could be used to probe the unpaired electrons in the dangling bonds at the plane termination.[72,73]

3. Conclusion

By interrogating the atomic displacement fields present in crystals of $MAPbBr_3$ using BDCI, we have identified that ⟨100⟩ edge dislocations are an important structural feature in halide perovskites, and that they are highly mobile under visible light illumination. Moreover, by intentionally studying a subset of crystals that are damaged by the X-ray beam, we discover that dislocation formation is a key feature of the halide perovskite degradation process, and that high dislocation densities correlate with a significant blue shift in the material's PL emission spectrum and a marked lengthening of its PL lifetime. Our results give a unique picture of the internal structure of halide perovskites and how it changes under device operation, elucidating the intimate links between nanoscale structure, dislocations, and device performance and stability. Such findings will be relevant for use of these micro-crystals and thin films in solar cells, photo-detectors, X-ray detectors, and LEDs, where defects have a direct influence on operational parameters.

Future work should focus on understanding the mechanism of dislocation migration and its relation to chemical and structural properties, including exploring why some halide perovskites show a greater propensity to degradation via dislocation formation than others. Computational calculations and atomic resolution electron microscopy have shown that in 2D WS_2, for example, highly mobile S atoms are instrumental in dislocation migration, and that this process has a remarkably low activation barrier.[74] Such an understanding of dislocation formation at the crystal growth stage will guide material and device fabrication procedures in order to avoid dislocation generation. Additional studies using BCDI to investigate the effect of applying external stress, for example, using strained epitaxy,[14] annealing/thermal expansion mismatch,[10,13] bending,[17] hydrostatic pressures,[75,76] among others, will be fruitful for developing controlled strain engineering in halide perovskites. Large single crystals are often used in certain device architectures for photodetectors[29,77] and X-ray detectors.[7,8] While the size of the crystals one can study with BCDI is limited to the coherence length of the X-ray beam and the sample-detector distance, techniques such as Bragg ptychography can be used to map internal nanoscale strains of more extended crystalline samples.[78] Nevertheless, BCDI is well suited to the study of individual grains in devices, and we propose that *operando* BCDI approaches under illumination, bias, humidity, temperature etc. could be used to study the evolution of intra-grain strain fields during device operation. This would provide an understanding of dislocation-grain boundary interactions and strain relaxation mechanisms, as well as a variety of other device-relevant photo-active structural changes in semiconductors.

4. Experimental Section

Sample Synthesis: Microcrystal film samples: Microcrystal film samples were synthesized by modifying the procedure reported by Saidaminov et al.[29,30,79] The glass/patterned ITO substrate was cleaned by sonicating in detergent, de-ionized water, acetone, and isopropyl alcohol for 10 min each. The substrate was then dried with a nitrogen blow-dry and exposed to UV ozone treatment for 10 min. Methylammonium lead bromide solution was prepared by dissolving MABr and $PbBr_2$ in a 1:1 molar ratio in 5 ml DMF solvent. The 1 M concentration solution was filtered with 0.45 µm PTFE filter and mixed with 1,2-dichlorobenzene, DCB, in a 5:4 volumetric ratio (DMF: DCB) to obtain precipitated $MAPbBr_3$ crystals. The microcrystal films were obtained by pouring the solution onto prepared substrates inside a small-capped petri dish and submerging the substrates. The petri dish was covered with a lid and the solution stirred at 500 rpm for 30 min at 40 °C. The coated substrates were then removed and annealed at 110 °C for 5 min to leave a microcrystal film.

Isolated microcrystals: Samples of isolated microcrystals were synthesized using a variation on the antisolvent vapor-assisted crystallization technique. SiN membranes (Silson Ltd., product number: SiRN-10.0-200-3.0-200) were placed in a petri dish that was then set inside a large crystallization basin containing chlorobenzene (Sigma Aldrich) antisolvent. 40 µL of precursor solution (0.1 M $PbBr_2$, 0.1 M MABr in 4:1 DMF:DMSO) were pipetted onto the SiN membrane, then the whole crystallization basin was covered with aluminum foil to slow the evaporation of chlorobenzene by partially trapping the vapor in the basin before escape. The chlorobenzene vapor dissolves in the precursor solution at a slow rate, encouraging $MAPbBr_3$ crystals to crash out of the solution.

BCDI Measurements: BCDI measurements were carried out at the I13-1 beamline of the Diamond Light Source (UK) using X-ray beam energies of 11.8 and 9.7 keV. Diffraction patterns were collected using the beamline's Excalibur photon-counting direct X-ray detector (Medipix3 chip) which was at a distance of 2.82 m from the sample. Measurements were taken in reflection geometry for microcrystals film samples, and were taken using a mixture of reflection and Laue (transmission) geometry for isolated crystal samples as these were on X-ray transparent SiN membranes. The beam is focused to a spot of ca. 2.5 µm in diameter. The crystals that became damaged under X-ray irradiation (e.g., in Figure 4) were measured using a beam energy of 9.7 keV (beam flux: $\approx 3 \times 10^7$ photons s^{-1}). Data for reconstructions shown in all other figures were measured with an X-ray energy of 11.8 keV (beam flux: $\approx 1 \times 10^7$ photons s^{-1}). At this energy, the proportion of crystals that suffered beam damage was smaller.

In a typical measurement, coherent diffraction patterns around the 100 Bragg peak were collected at 51 rocking curve angles separated by 0.005°

(spanning a total angle range of 0.25°) with a collection dwell time of 10 s at each rocking curve angle. $MAPbBr_3$ is cubic at the temperature at which these measurements were performed, i.e., room temperature.

To perform the measurements under illumination we constructed a home-built light-soaking rig on the beamline with a 405 nm continuous wave diode laser (CNI, model MLL-III-405) coupled to an optical fiber via a collimating lens. The laser power was tuned to achieve a ≈1 sun intensity (in terms of photo-generated charge carriers) at the sample position. The power at this position was measured using a portable power meter (Thorlabs PM100D console unit; S120C Si photodiode power sensor).

Electron Density Reconstruction: The measured coherent diffraction patterns were fast Fourier transformed back to real-space to get the crystal reconstructions. The amplitude was restored by taking the square root of the intensity, while the phase was retrieved using iterative phasing methods. A linear combination of typical iterative phasing algorithms was used, including Error Reduction (ER), Hybrid Input-output (HIO),[32] and relaxed averaged alternating reflection (RAAR)[80] algorithms. The shrink-wrap[33] method was applied for updating the real-space constraints during the iterations and guided algorithms[81] were turned on for selecting the solution with minimum sharpness after each generation. Each diffraction pattern was reconstructed ten times with random initial guess to ensure reproducibility.

Reconstructions shown in this work are isovolumes whose surface is determined by setting a threshold value of electron density modulus and not displaying regions of space with modulus lower than this threshold value. For most reconstructions, a threshold of 0.1 was used (reconstructed electron density functions are normalized between 0 and 1).

Determination of Burgers Vector Magnitudes: Electron density reconstructions were produced in .vtk file format and viewed and analyzed using the open-source Preview[82] data visualization software. Slices through the reconstruction were taken perpendicular (by eye) to the dislocation line and then displacement values were extracted along circular paths centered on the dislocation core at three different radii, *r*. Note that *r* should be small enough so the strain field from the dislocation dominates any contribution from other strain fields present in the crystal, but large enough not to be on the dislocation core. The resulting displacement versus arc angle data was fit according to the function given in the main text using the SciPy Python package. The three calculated Burgers vector magnitudes were then averaged.

Hyperspectral PL Microscopy: A Photon Etc. IMA Vis microscope was used for the wide-field hyperspectral microscopy studies with 100X Olympus and 50X Nikon aberration-corrected objective lenses in place. Sample excitation was achieved using a 405 nm continuous wave laser filtered with a dichroic mirror. Spectral resolution is achieved since the emitted light from the sample is spectrally split through a volume Bragg grating before being collected by a charged-coupled device (CCD) camera. The camera used is a 2048 × 2048 resolution Hamamatsu Orca Flash V3.0 with a wavelength range of 400–1000 nm and is maintained at −10 °C during measurements. The position on the sample from which light is emitted is calculated by scanning the angle of the grating relative to the emitted light.

In a typical measurement, PL is collected from an area of 89 μm × 89 μm using a (wide field) incident laser intensity of 30 μW cm^{-2} and a dwell time of 10 s at each collection wavelength.

Confocal PL Microscopy: Fluorescence lifetime imaging maps were acquired with a MicroTime200 laser scanning confocal microscope set-up from Picoquant. Fluorescence was excited with a 509 nm diode laser (LDH-D-C-510, Picoquant; 2.96 MHz) using a 100 × 0.9 NA objective (Olympus MPlanFL N). The PL was collected in reflection geometry, sent through a pinhole of 100 μm diameter, and detected with an Excelitas SPAD detector. The system has an approximate time resolution of 400 ps. Unwanted scattering from the excitation laser is suppressed by a combination of a long-pass dichroic mirror and a 519 nm long-pass filter.

In a typical measurement, an area of 10 × 10 μm was divided into 256 × 256 pixels with a dwell time of 10 μs. The eventual image is calculated as the sum of 200 complete scans. For the measurements shown in Figure 4f, a laser power of 4.7 nW was used with a repetition rate of 20 MHz for the pristine crystals, and 8 MHz for the damaged crystals. The spot diameter is estimated using the airy disc diameter of $1.22 \times \frac{\lambda}{NA}$.

Supporting Information

Supporting Information is available from the Wiley Online Library or from the author.

Acknowledgements

K.W.P.O. acknowledges an EPSRC studentship (project reference: 2275833). J.D. thanks the China Scholarship Council (CSC) for financial support. M.N.L and O.M.B. acknowledge financial support from KAUST. A.N.I. acknowledges scholarships from the British Spanish Society, Sir Richard Stapley Educational Trust, and the Rank Prize Fund. S.K. acknowledges funding from the Leverhulme Trust (ECF-2022-593), the Isaac Newton Trust (22.08(i)), and the German Academic Foreign Service (91793256). K.F. acknowledges a Winton Sustainability Fund Studentship, a George and Lilian Schiff Studentship, and an Engineering and Physical Sciences Research Council (EPSRC) studentship. M.D. acknowledges Leverhulme Research Grant RPG-2021-191. S.J.Z. acknowledges support from the Polish National Agency for Academic Exchange within the Bekker program (grant no. PPN/BEK/2020/1/00264/U/00001). A.E.D. Acknowledges funding from EPSRC Cambridge NanoDTC, EP/L015978/1. T.A.S. Acknowledges funding from EPSRC Cambridge NanoDTC, EP/S022953/1. T.A.S.D. acknowledges the support of an Ernest Oppenheimer Early Career Fellowship and a Schmidt Science Fellowship. S.H. acknowledges funding from EPSRC (EP/T001038/1). I.K.R. acknowledges support from the U.S. Department of Energy, Office of Science, Office of Basic Energy Sciences, under Contract No. DE-SC0012704 and EPSRC. S.D.S. acknowledges the Royal Society and Tata Group (grant no. UF150033). The work has received funding from the European Research Council under the European Union's Horizon 2020 research and innovation program (HYPERION, grant agreement no. 756962). The authors acknowledge the EPSRC (EP/R023980/1, EP/S030638/1) for funding. The authors acknowledge Diamond Light Source for time on Beamline I13-1 under proposal numbers MG25097-1, MG28495-1, and MG30308-1. Work at Brookhaven National Laboratory was supported by the U.S. Department of Energy, Office of Science, Office of Basic Energy Sciences, under Contract No. DE-SC0012704. Work performed at UCL was supported by EPSRC. For the purpose of open access, the author has applied a Creative Commons Attribution (CC BY) license to any Author Accepted Manuscript version arising.

Conflict of Interest

S.D.S. is a cofounder of Swift Solar.

Author Contributions

S.D.S., I.K.R., T.A.S.D., and K.W.P.O. conceived of the project. K.W.P.O, J.D., D.J.B, A.N.I., S.K., K.F., M.D., S.J.Z., A.E.D., T.A.S., and P.L. carried out the BCDI measurements. J.D. generated the crystal reconstructions, which were analyzed by K.W.P.O. K.W.P.O. carried out the hyperspectral and confocal photoluminescence microscopy measurements. M.N.L. prepared the microcrystal film samples and K.W.P.O. prepared the isolated microcrystal samples. A.E.D. synthesized the large flat microcrystal samples. S.D.S. supervised K.W.P.O., A.N.I., K.F., T.A.S., and T.A.S.D. I.K.R. supervised J.D. O.B. supervised M.N.L. S.D.S. and S.H. supervised A.E.D. K.W.P.O. produced first drafts and all authors contributed to editing the manuscript.

Data Availability Statement

The data that support the findings of this study are openly available in Apollo at https://doi.org/10.17863/CAM.101790.[83]

Keywords

coherent X-ray diffraction imaging, dislocations, halide perovskite

Received: June 9, 2023
Revised: September 1, 2023
Published online:

[1] J. Burschka, N. Pellet, S.-J. Moon, R. Humphry-Baker, P. Gao, M. K. Nazeeruddin, M. Grätzel, *Nature* **2013**, *499*, 316.
[2] "Best Research-Cell Efficiency Chart," can be found under https://www.nrel.gov/pv/cell-efficiency.html, n.d. (accessed: September 2023).
[3] J. S. Kim, J.-M. Heo, G.-S. Park, S.-J. Woo, C. Cho, H. J. Yun, D.-H. Kim, J. Park, S.-C. Lee, S.-H. Park, E. Yoon, N. C. Greenham, T.-W. Lee, *Nature* **2022**, *611*, 688.
[4] Y. Dong, Y.-K. Wang, F. Yuan, A. Johnston, Y. Liu, D. Ma, M.-J. Choi, B. Chen, M. Chekini, S.-W. Baek, L. K. Sagar, J. Fan, Y. Hou, M. Wu, S. Lee, B. Sun, S. Hoogland, R. Quintero-Bermudez, H. Ebe, P. Todorovic, F. Dinic, P. Li, H. T. Kung, M. I. Saidaminov, E. Kumacheva, E. Spiecker, L.-S. Liao, O. Voznyy, Z.-H. Lu, E. H. Sargent, *Nat. Nanotechnol.* **2020**, *15*, 668.
[5] T. Chiba, Y. Hayashi, H. Ebe, K. Hoshi, J. Sato, S. Sato, Y.-J. Pu, S. Ohisa, J. Kido, *Nat. Photonics* **2018**, *12*, 681.
[6] Y. Sun, L. Ge, L. Dai, C. Cho, J. Ferrer Orri, K. Ji, S. J. Zelewski, Y. Liu, A. J. Mirabelli, Y. Zhang, J.-Y. Huang, Y. Wang, K. Gong, M. C. Lai, L. Zhang, D. Yang, J. Lin, E. M. Tennyson, C. Ducati, S. D. Stranks, L.-S. Cui, N. C. Greenham, *Nature* **2023**, *615*, 830.
[7] K. Sakhatskyi, B. Turedi, G. J. Matt, E. Wu, A. Sakhatska, V. Bartosh, M. N. Lintangpradipto, R. Naphade, I. Shorubalko, O. F. Mohammed, S. Yakunin, O. M. Bakr, M. V. Kovalenko, *Nat. Photonics* **2023**, *17*, 510.
[8] H. Wei, J. Huang, *Nat. Commun.* **2019**, *10*, 1066.
[9] T. W. Jones, A. Osherov, M. Alsari, M. Sponseller, B. C. Duck, Y.-K. Jung, C. Settens, F. Niroui, R. Brenes, C. V. Stan, Y. Li, M. Abdi-Jalebi, N. Tamura, J. E. Macdonald, M. Burghammer, R. H. Friend, V. Bulovic, A. Walsh, G. J. Wilson, S. Lilliu, S. D. Stranks, *Energy Environ. Sci.* **2019**, *12*, 596.
[10] C. Zhu, X. Niu, Y. Fu, N. Li, C. Hu, Y. Chen, X. He, G. Na, P. Liu, H. Zai, Y. Ge, Y. Lu, X. Ke, Y. Bai, S. Yang, P. Chen, Y. Li, M. Sui, L. Zhang, H. Zhou, Q. Chen, *Nat. Commun.* **2019**, *10*, 815.
[11] K. Frohna, M. Anaya, S. Macpherson, J. Sung, T. A. S. Doherty, Y.-H. Chiang, A. J. Winchester, K. W. P. Orr, J. E. Parker, P. D. Quinn, K. M. Dani, A. Rao, S. D. Stranks, *Nat. Nanotechnol.* **2021**, 1.
[12] D.-J. Xue, Y. Hou, S.-C. Liu, M. Wei, B. Chen, Z. Huang, Z. Li, B. Sun, A. H. Proppe, Y. Dong, M. I. Saidaminov, S. O. Kelley, J.-S. Hu, E. H. Sargent, *Nat. Commun.* **2020**, *11*, 1514.
[13] X. Li, Y. Luo, M. V. Holt, Z. Cai, D. P. Fenning, *Chem. Mater.* **2019**, *31*, 2778.
[14] Y. Chen, Y. Lei, Y. Li, Y. Yu, J. Cai, M.-H. Chiu, R. Rao, Y. Gu, C. Wang, W. Choi, H. Hu, C. Wang, Y. Li, J. Song, J. Zhang, B. Qi, M. Lin, Z. Zhang, A. E. Islam, B. Maruyama, S. Dayeh, L.-J. Li, K. Yang, Y.-H. Lo, S. Xu, *Nature* **2020**, *577*, 209.
[15] X. Zheng, C. Wu, S. K. Jha, Z. Li, K. Zhu, S. Priya, *ACS Energy Lett.* **2016**, *1*, 1014.
[16] D. Liu, D. Luo, A. N. Iqbal, K. W. P. Orr, T. A. S. Doherty, Z.-H. Lu, S. D. Stranks, W. Zhang, *Nat. Mater.* **2021**, *20*, 1337.
[17] J. Zhao, Y. Deng, H. Wei, X. Zheng, Z. Yu, Y. Shao, J. E. Shield, J. Huang, *Sci. Adv.* **2017**, *3*, eaao5616.
[18] E. M. Tennyson, T. A. S. Doherty, S. D. Stranks, *Nat. Rev. Mater.* **2019**, *4*, 573.
[19] P. Quinn, J. Parker, F. Cacho-Nerin, M. Walker, P. Howes, *Microsc. Microanal.* **2018**, *24*, 244.
[20] M. U. Rothmann, J. S. Kim, J. Borchert, K. B. Lohmann, C. M. O'leary, A. A. Sheader, L. Clark, H. J. Snaith, M. B. Johnston, P. D. Nellist, L. M. Herz, *Science* **2020**, *370*, eabb5940.
[21] K. Song, J. Liu, N. Lu, D. Qi, W. Qin, *Phys. Chem. Chem. Phys.* **2022**, *24*, 6393.
[22] J. S. Barnard, J. Sharp, J. R. Tong, P. A. Midgley, *Science* **2006**, *313*, 319.
[23] M. C. Newton, S. J. Leake, R. Harder, I. K. Robinson, *Nat. Mater.* **2010**, *9*, 120.
[24] J. Diao, X. Shi, T. A. Assefa, L. Wu, A. F. Suzana, D. S. Nunes, D. Batey, S. Cipiccia, C. Rau, R. J. Harder, W. Cha, I. K. Robinson, *Phys. Rev.* **2020**, *4*, 106001.
[25] D. Dzhigaev, Z. Zhang, L. A. B. Marçal, S. Sala, A. Björling, A. Mikkelsen, J. Wallentin, *New J. Phys.* **2021**, *23*, 063035.
[26] D. Dzhigaev, Y. Smirnov, P.-A. Repecaud, L. A. B. Marçal, G. Fevola, D. Sheyfer, Q. Jeangros, W. Cha, R. Harder, A. Mikkelsen, J. Wallentin, M. Morales-Masis, M. E. Stuckelberger, *Commun. Mater.* **2022**, *3*, 38.
[27] J. N. Clark, J. Ihli, A. S. Schenk, Y.-Y. Kim, A. N. Kulak, J. M. Campbell, G. Nisbet, F. C. Meldrum, I. K. Robinson, *Nat. Mater.* **2015**, *14*, 780.
[28] A. Ulvestad, A. Singer, J. N. Clark, H. M. Cho, J. W. Kim, R. Harder, J. Maser, Y. S. Meng, O. G. Shpyrko, *Science* **2015**, *348*, 1344.
[29] M. I. Saidaminov, V. Adinolfi, R. Comin, A. L. Abdelhady, W. Peng, I. Dursun, M. Yuan, S. Hoogland, E. H. Sargent, O. M. Bakr, *Nat. Commun.* **2015**, *6*, 8724.
[30] M. I. Saidaminov, M. d. A. Haque, M. Savoie, A. L. Abdelhady, N. Cho, I. Dursun, U. Buttner, E. Alarousu, T. Wu, O. M. Bakr, *Adv. Mater.* **2016**, *28*, 8144.
[31] H. N. Chapman, K. A. Nugent, *Nat. Photonics* **2010**, *4*, 833.
[32] J. R. Fienup, *Appl. Opt.* **1982**, *21*, 2758.
[33] S. Marchesini, *Rev. Sci. Instrum.* **2007**, *78*, 011301.
[34] I. K. Robinson, I. A. Vartanyants, *Appl. Surf. Sci.* **2001**, *182*, 186.
[35] I. A. Vartanyants, I. K. Robinson, *J. Phys.: Condens. Matter* **2001**, *13*, 10593.
[36] A. Chen, M. Yossef, C. Zhang, *Sol. Energy* **2018**, *163*, 243.
[37] C. Yang, K. Song, X. Xu, G. Yao, Z. Wu, *Sol. Energy* **2020**, *195*, 121.
[38] D. Hull, D. J. Bacon, *Introduction to Dislocations*, Elsevier Science & Technology, Oxford, United Kingdom **2011**.
[39] P. M. Anderson, J. P. Hirth, J. Loethe, *Theory of Dislocations*, Cambridge University Press, New York, NY, **2017**.
[40] J. Feng, *APL Mater.* **2014**, *2*, 081801.
[41] A. Jaffe, Y. Lin, C. M. Beavers, J. Voss, W. L. Mao, H. I. Karunadasa, *ACS Cent. Sci.* **2016**, *2*, 201.
[42] B. Yang, W. Ming, M.-H. Du, J. K. Keum, A. A. Puretzky, C. M. Rouleau, J. Huang, D. B. Geohegan, X. Wang, K. Xiao, *Adv. Mater.* **2018**, *30*, 1705801.
[43] H. Zhang, Y. Liu, H. Lu, W. Deng, K. Yang, Z. Deng, X. Zhang, S. Yuan, J. Wang, J. Niu, X. Zhang, Q. Jin, H. Feng, Y. Zhan, L. Zheng, *Appl. Phys. Lett.* **2017**, *111*, 103904.
[44] S. Jariwala, H. Sun, G. W. P. Adhyaksa, A. Lof, L. A. Muscarella, B. Ehrler, E. C. Garnett, D. S. Ginger, *Joule* **2019**, *3*, 3048.
[45] A. Walsh, S. D. Stranks, *ACS Energy Lett.* **2018**, *3*, 1983.
[46] J. Xing, Q. Wang, Q. Dong, Y. Yuan, Y. Fang, J. Huang, *Phys. Chem. Chem. Phys.* **2016**, *18*, 30484.
[47] D. W. Dequilettes, W. Zhang, V. M. Burlakov, D. J. Graham, T. Leijtens, A. Osherov, V. Bulovic, H. J. Snaith, D. S. Ginger, S. D. Stranks, *Nat. Commun.* **2016**, *7*, 11683.
[48] G. Y. Kim, A. Senocrate, T.-Y. Yang, G. Gregori, M. Grätzel, J. Maier, *Nat. Mater.* **2018**, *17*, 445.
[49] Y. Yuan, J. Huang, *Acc. Chem. Res.* **2016**, *49*, 286.
[50] J. W. Kim, A. Ulvestad, S. Manna, R. Harder, E. E. Fullerton, O. G. Shpyrko, *Nanoscale* **2017**, *9*, 13153.
[51] I. C. Kaya, K. P. S. Zanoni, F. Palazon, M. Sessolo, H. Akyildiz, S. Sonmezoglu, H. J. Bolink, *Adv. Energy Sustainability Res.* **2021**, *2*, 2000065.

[52] E. Mosconi, D. Meggiolaro, H. J. Snaith, S. D. Stranks, F. De Angelis, *Energy Environ. Sci.* **2016**, *9*, 3180.
[53] N. Phung, A. Mattoni, J. A. Smith, D. Skroblin, H. Köbler, L. Choubrac, J. Breternitz, J. Li, T. Unold, S. Schorr, C. Gollwitzer, I. G. Scheblykin, E. L. Unger, M. Saliba, S. Meloni, A. Abate, A. Merdasa, *Joule* **2022**, *6*, 2152.
[54] J. Ferrer Orri, T. A. S. Doherty, D. Johnstone, S. M. Collins, H. Simons, P. A. Midgley, C. Ducati, S. D. Stranks, *Adv. Mater.* **2022**, *34*, 2200383.
[55] Y. Zhou, J. Chen, O. M. Bakr, O. F. Mohammed, *ACS Energy Lett.* **2021**, *6*, 739.
[56] O. D. I. Moseley, T. A. S. Doherty, R. Parmee, M. Anaya, S. D. Stranks, *J. Mater. Chem. C* **2021**, *9*, 11588.
[57] J. Ihli, J. N. Clark, A. S. Côté, Y.-Y. Kim, A. S. Schenk, A. N. Kulak, T. P. Comyn, O. Chammas, R. J. Harder, D. M. Duffy, I. K. Robinson, F. C. Meldrum, *Nat. Commun.* **2016**, *7*, 11878.
[58] N. Rolston, K. A. Bush, A. D. Printz, A. Gold-Parker, Y. Ding, M. F. Toney, M. D. Mcgehee, R. H. Dauskardt, *Adv. Energy Mater.* **2018**, *8*, 1802139.
[59] I. Yonenaga, K. Sumino, *J. Appl. Phys.* **1993**, *73*, 1681.
[60] D. Maroudas, R. A. Brown, *J. Appl. Phys.* **1991**, *69*, 3865.
[61] M. Kittler, M. Reiche, *Structure and Properties of Dislocations in Silicon*, InTech, London **2011**.
[62] I. Nikiforov, D.-B. Zhang, T. Dumitrica, *J. Phys. Chem. Lett.* **2011**, *2*, 2544.
[63] S. E. Bennett, *Mater. Sci. Technol.* **2010**, *26*, 1017.
[64] J. W. Matthews, T. S. Plaskett, S. E. Blum, *J. Cryst. Growth* **1977**, *42*, 621.
[65] D. Laister, G. M. Jenkins, *J. Mater. Sci.* **1970**, *5*, 862.
[66] K. Ishida, M. Akiyama, S. Nishi, *Jpn. J. Appl. Phys.* **1987**, *26*, L163.
[67] G. C. Kuczynski, K. R. Iyer, C. W. Allen, *J. Appl. Phys.* **1972**, *43*, 1337.
[68] T. Suzuki, S. Takeuchi, H. Yoshinaga, in *Dislocation Dynamics and Plasticity* (Eds.: T. Suzuki, S. Takeuchi, H. Yoshinaga), Springer, Berlin, Heidelberg **1991**, pp. 99–119.
[69] M. L. Trunov, *J. Phys. D: Appl. Phys.* **2008**, *41*, 074011.
[70] W. T. Read, *Lond. Edinb. Dublin Philos. Mag. J. Sci.* **1954**, *45*, 775.
[71] J. B. Clarke, J. W. Hastie, L. H. E. Kihlborg, R. Metselaar, M. M. Thackeray, *Pure Appl. Chem.* **1994**, *66*, 577.
[72] H. Alexander, C. Kisielowski-Kemmerich, E. R. Weber, *Physica* **1983**, *116*, 583.
[73] A. M. Stoneham, *J. Phys. C: Solid State Phys.* **1974**, *7*, 871.
[74] A. Azizi, X. Zou, P. Ercius, Z. Zhang, A. L. Elías, N. Perea-López, G. Stone, M. Terrones, B. I. Yakobson, N. Alem, *Nat. Commun.* **2014**, *5*, 4867.
[75] G. Liu, L. Kong, J. Gong, W. Yang, H.-K. Mao, Q. Hu, Z. Liu, R. D. Schaller, D. Zhang, T. Xu, *Adv. Funct. Mater.* **2017**, *27*, 1604208.
[76] X. Lü, Y. Wang, C. C. Stoumpos, Q. Hu, X. Guo, H. Chen, L. Yang, J. S. Smith, W. Yang, Y. Zhao, H. Xu, M. G. Kanatzidis, Q. Jia, *Adv. Mater.* **2016**, *28*, 8663.
[77] G. Maculan, A. D. Sheikh, A. L. Abdelhady, M. I. Saidaminov, M. A. Haque, B. Murali, E. Alarousu, O. F. Mohammed, T. Wu, O. M. Bakr, *J. Phys. Chem. Lett.* **2015**, *6*, 3781.
[78] F. Pfeiffer, *Nat. Photonics* **2018**, *12*, 9.
[79] C. Stavrakas, A. A. Zhumekenov, R. Brenes, M. Abdi-Jalebi, V. Bulovic, O. M. Bakr, E. S. Barnard, S. D. Stranks, *Energy Environ. Sci.* **2018**, *11*, 2846.
[80] D. R. Luke, *Inverse Probl.* **2004**, *21*, 37.
[81] C.-C. Chen, J. Miao, C. W. Wang, T. K. Lee, *Phys. Rev. B* **2007**, *76*, 064113.
[82] J. Ahrens, B. Geveci, C. Law, *ParaView: An End-User Tool for Large Data Visualization*, Elsevier, New York **2005**.
[83] K. W. P. Orr, J. Diao, M. N. Lintangpradipto, D. J. Batey, A. N. Iqbal, S. Kahmann, K. Frohna, M. Dubajic, S. J. Zelewski, A. E. Dearle, T. A. Selby, P. Li, T. A. S. Doherty, S. Hofmann, O. M. Bakr, I. K. Robinson, S. D. Stranks, **2023**, Research data supporting 'Imaging Light-Induced Migration of Dislocations in Halide Perovskites with 3D Nanoscale Strain Mapping', Apollo - University of Cambridge Repository.